New approach to description of (d, xn) spectra at energies below 50 MeV in Monte Carlo simulation by intra-nuclear cascade code with Distorted Wave Born Approximation

S. Hashimoto [a,*], Y. Iwamoto [a], T. Sato [a], K. Niita [b], A. Boudard [c], J. Cugnon [d], J.-C. David [c], S. Leray [c], D. Mancusi [c]

[a] Japan Atomic Energy Agency, Ibaraki-ken 319-1195, Japan
[b] Research Organization for Information Science and Technology, Ibaraki-ken 319-1196, Japan
[c] CEA, Centre de Saclay, IRFU/Service de Physique Nucléaire, F-91191 Gif-sur-Yvette, France
[d] Fundamental Interactions in Physics and Astrophysics, University of Liège, allée du 6 août 17, bât. B5, B-4000 Liège 1, Belgium

ARTICLE INFO

ABSTRACT

A new approach to describing neutron spectra of deuteron-induced reactions in the Monte Carlo simulation for particle transport has been developed by combining the Intra-Nuclear Cascade of Liège (INCL) and the Distorted Wave Born Approximation (DWBA) calculation. We incorporated this combined method into the Particle and Heavy Ion Transport code System (PHITS) and applied it to estimate (d, xn) spectra on ^{nat}Li, ^{9}Be, and ^{nat}C targets at incident energies ranging from 10 to 40 MeV. Double differential cross sections obtained by INCL and DWBA successfully reproduced broad peaks and discrete peaks, respectively, at the same energies as those observed in experimental data. Furthermore, an excellent agreement was observed between experimental data and PHITS-derived results using the combined method in thick target neutron yields over a wide range of neutron emission angles in the reactions. We also applied the new method to estimate (d, xp) spectra in the reactions, and discussed the validity for the proton emission spectra.

© 2014 Elsevier B.V. All rights reserved.

1. Introduction

Accelerator-based neutron sources have been the focus of scientific research and medical applications such as the International Fusion Materials Irradiation Facility (IFMIF) project [1] and Boron Neutron Capture Therapy (BNCT). To produce high-intensity neutron beams required for such applications, deuteron-induced reactions of Li, Be, or C targets at low (<50 MeV) incident energies are essential.

In the design of radiation facilities, computer codes for particle transport simulation based on the Monte Carlo technique play an important role in estimating particle fluxes or dose distributions in the radiation fields. A critical part of such simulation codes is the description of behavior of primary and secondary particles after nuclear reaction processes in particle collisions using a nuclear reaction model. The accuracy of the model determines the reliability of the results obtained from the simulation because the particle yields, spectra, and dose distributions depend on the

features included in the model. The Particle and Heavy Ion Transport code System (PHITS) [2], one of the Monte Carlo simulation codes, has been successfully applied to estimate particle fluxes or radiation dose in accelerator design [3], radiation therapy[4], and cosmic-ray science [5,6], using nuclear reaction models such as the Jet AA Microscopic transport (JAM) model [7] and the JAERI Quantum Molecular Dynamics (JQMD) model [8]. However, these models do not operate well in a low-energy region (i.e., below 100 MeV), and JQMD, which has been used for nucleus–nucleus collisions, is especially insufficient for deuteron-induced reactions, as shown in Ref. [9].

For the design of neutron sources or radiation shielding, it is important to adequately describe the reaction processes induced by neutrons as well as deuterons. However, PHITS can only use experimental data of double differential cross sections (DDXs) as neutron sources from the deuteron-induced reaction, since JQMD cannot reproduce the required data. The simulation with the option using the experimental data directly can be performed only for limited incident energies.

Therefore, we have developed a new method for nuclear reaction modeling that combines the Intra-Nuclear Cascade of Liège

---

(INCL) [10–12] and Distorted Wave Born Approximation (DWBA). INCL can reproduce a broad peak at half the incident deuteron energy in an inclusive (d, xn) spectrum at forward angles, since it considers a proton-stripping process, where the proton inside the deuteron interacts with a target nucleus strongly while the neutron flies out. This process is the dominant contributor to the peak, as shown in Ref. [13] using the Glauber model. Furthermore, discrete peaks appearing in the high energy region of the spectrum are included in the DWBA results; these peaks correspond to transitions between a ground state of target nuclei and a ground or excited state of a residual nucleus. This method was applied to reproduce the neutron spectrum in deuteron-induced reactions on Li and Be at 40 and 18 MeV, respectively [14]. The results obtained by using the method were found to be in good agreement with experimental data for thin and thick targets. In this paper, we present the details of the method and the calculation, and discuss results for the reactions on Li, Be, and C at low (<50 MeV) incident energies.

Furthermore, we discuss the applicability of the method to estimating proton emission spectra in the deuteron-induced reactions. The proton spectra have a similar shape to the neutron spectra. Ye et al. [15] demonstrated that a neutron-stripping process is the dominant contributor to the broad peak of the proton spectra at forward angles. INCL includes the process by the similar way to the proton-stripping. In addition, discrete peaks can be considered in the method by using DWBA. In the present study, we also estimate DDXs in the (d, xp) reaction to discuss the validity of the method for the proton emission.

2. New combined method

2.1. INCL

Here, we explain INCL only as it relates to the present study. See Refs. [10,11] for details about the reaction mechanisms considered by INCL. Although the latest version of INCL (version 4.6) was described in Ref. [12], we used the version 4.5 of INCL in this study, because the version 4.5 is more effective in reproducing neutron spectra in the deuteron-induced reactions below 50 MeV than version 4.6.

In the combined method, the majority of the overall nuclear reaction cross section is represented by INCL. Since INCL deals with nucleons as well as deuterons or other light ions as incident particles, it can suitably reproduce the (d, xn) spectrum. INCL, developed by the University of Liège (Belgium) and CEA-Saclay (France), considers various physical features and can successfully reproduce many observables for a wide range of incident energies and target nucleus regions.

For the deuteron-induced reactions, INCL initially generates the spatial and momentum distributions of nucleons inside the deuteron, imposing that the sum of their momenta equals to 0 in the c.m. system of the deuteron. The spatial distribution is assumed to be Gaussian with the root mean square radius of the deuteron, and the momentum distribution is calculated with the Paris potential [16]. In order to obtain a correct total incident energy, namely to satisfy the energy conservation law, the nucleons of the deuteron are boosted with a velocity such that the total kinetic energy is the same as the nominal deuteron kinetic energy diminished by the deuteron binding energy. This velocity is slightly smaller than the deuteron nominal velocity, by a fraction of the order of the ratio between the binding energy and the kinetic energy of the incident deuteron. In the present case, this assumption works well, because deuterons are loosely bound nuclei. See Ref. [10] for details. Initial spatial and momentum distributions of target nucleons are generally described using the Woods–Saxon form and the uniform Fermi sphere approximation, respectively. However, for

light targets ($A < 18$, where A is the target mass number), such as those considered in this paper, a modified harmonic oscillator or a Gaussian form is used for the position distribution [11]. Considering these initial conditions, the cascade process is described by successive nucleon–nucleon collisions.

Although we consider deuteron-induced reactions at energies below the applicable range of INCL, with respect to the incident energy, this model gives surprisingly good descriptions of broad peaks observed in neutron spectra at forward angles, as will be shown later. This is possibly because INCL includes the proton-stripping process, the validity of which was confirmed in the reproduction of (d, xn) spectra on Pb at 1600 MeV [10]. The elastic deuteron breakup process, which is not included in INCL, also contributes to the broad peaks. However, we neglected this process in this study since its contribution to the peaks is expected to be smaller than that from the proton-stripping process, especially at forward angles. Ye et al. [13] verified this by comparing cross sections of the proton-stripping process calculated by the Glauber model with those of the elastic breakup obtained by the continuum-discretized coupled-channels method (CDCC) [17,18]. It should be noted that the contribution of the elastic breakup should not be neglected for heavy targets in the low-energy region because of the enhancement of the so-called Coulomb breakup, unlike light targets which we deals with here.

2.2. DWBA

Some discrete peaks generally observed in inclusive (d, xn) and (d, xp) spectra at forward angles are attributed to the transitions between a discrete state of a target nucleus and that of a residue. DWBA is a quantum mechanical method for obtaining probabilities (i.e., cross sections) of such transitions and has been used in analyzing many types of nuclear reactions since it is a relatively convenient model in the Born approximation. With DWBA, the angular distribution of the cross section has interference patterns because of quantum mechanical effects.

We performed DWBA of the two transfer reaction with the deuteron incident, (d, n) and (d, p), using the TWO-FNR code [19]. This code has been applied to analyze various transfer reactions [20–23]. In this study, we assumed that the transfer process occurs in only one step on the basis of the three-body model, as shown in Fig. 1. Therefore, the effects of multi-step processes and internal multi-nucleon systems in the target nucleus are neglected.

Under this assumption, the angular differential cross section is given by

$$\frac{d\sigma}{d\Omega} = F|T_{\text{DWBA}}|^2, \tag{1}$$

where F is a kinematical factor, and T_{DWBA} is the transition matrix element of DWBA. The matrix element for the (d, n) reaction is described by
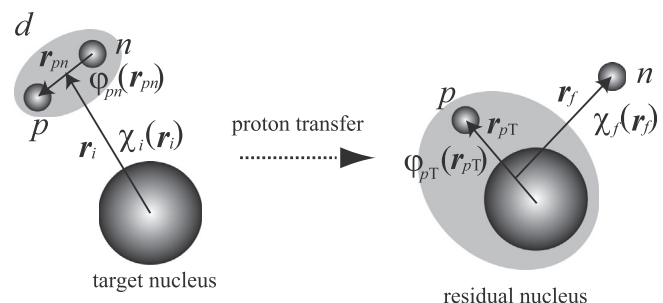

Fig. 1. Coordinate system of the three-body model in DWBA for the (d, n) reaction and wave functions, $\chi_i(\mathbf{r}_i)$, $\chi_f(\mathbf{r}_f)$, $\varphi_{pn}(\mathbf{r}_{pn})$, and $\varphi_{pT}(\mathbf{r}_{pT})$.

$$T_{\text{DWBA}} = N\langle \chi_f \varphi_{p\text{T}} | V_{pn} | \varphi_{pn} \chi_i \rangle. \tag{2}$$

Here, N is a normalization factor, $\chi_i(\boldsymbol{r}_i)$ and $\chi_f(\boldsymbol{r}_f)$ are distorted waves between d and the target nucleus in the initial state and n and the residual nucleus in the final state, respectively, $\varphi_{pn}(\boldsymbol{r}_{pn})$ is the internal wave function of d, $\varphi_{p\text{T}}(\boldsymbol{r}_{p\text{T}})$ is the bound state wave function of p in the residual nucleus, and $V_{pn}(\boldsymbol{r}_{pn})$ is the residual interaction for the proton transfer reaction. The distorted wave χ_i (χ_f) is a solution of the Schrödinger equation with an optical potential between d and the target (n and the residue). The form of the optical potential used in the present study is

$$U(r) = -V_0 f(x_{\text{V}}) - 4iW_0 g(x_{\text{Wd}}) - 2\left(\frac{\hbar}{m_\pi c}\right)^2 \frac{V_{\text{SO}}}{a_{\text{SO}} r} g(x_{\text{SO}})\boldsymbol{l}\cdot\boldsymbol{s} + V_{\text{C}}(r), \tag{3}$$

where

$$f(x_i) = (1 + e^{x_i})^{-1}, g(x_i) = e^{x_i}(1 + e^{x_i})^{-2},$$
$$x_i = (r - r_i A^{1/3})/a_i \quad (i = \text{V}, \text{Wd}, \text{SO}). \tag{4}$$

Here, $V_{\text{C}}(r)$ is the Coulomb potential with a uniformly charged sphere of radius $r_{\text{V}} A^{1/3}$. The bound state $\varphi_{p\text{T}}$ is also a solution of the Schrödinger equation with a single-particle potential, which is similar to Eq. (3) after neglecting the imaginary part. To obtain results for a specified binding energy, the code uses the potential depth search procedure, where only the strength of the central part V_0 is searched and that of the spin–orbit term V_{SO} is fixed. In this study, we set $V_{\text{SO}} = 6.0$ MeV, $r_{\text{V}} = r_{\text{SO}} = 1.25$ fm, and $a_{\text{V}} = a_{\text{SO}} = 0.65$ fm. Furthermore, we used the zero-range approximation,

$$V_{pn}(\boldsymbol{r}_{pn})\varphi_{pn}(\boldsymbol{r}_{pn}) \sim D_0\delta(\boldsymbol{r}_{pn}), \tag{5}$$

with the strength of $D_0^2 = 1.53 \times 10^4$ MeV^2 fm^3, since the finite range effect appears small compared with the uncertainty in optical potential parameters. Here, we have described in details the DWBA calculation only for the (d, n) reaction and have omitted the description of that for the (d, p) reaction, because the latter can be obtained by the interchange of the neutron and proton in the above equations.

Table 1 presents reaction channels of (d, n) transitions, used in this study, to consider inclusive neutron spectra on ^{6,7}Li, ^{9}Be, and ^{12,13}C targets. It shows excitation energies E_{ex} and decay widths Γ of the final states of residual nuclei, reaction Q-values, transferred total angular momentum j, and normalization factors N of each reaction. Decay widths are used to reproduce a width of a discrete peak corresponding to each transition in the PHITS calculation. The value of Γ for stable ground states is 0. Furthermore, for long-lived states with half-life τ of longer than 0.658 fs, Γ is also set to 0. The value of τ relates with Γ as follows: $\tau[\text{fs}] = 0.658/\Gamma[\text{eV}]$. One-proton separation energies S_p for d, ^{7}Be, ^{8}Be, ^{10}B, ^{13}N, and ^{14}N, are 2.23, 5.61, 17.26, 6.59, 1.94, and 7.55 MeV, respectively, and Q-values are calculated from these separation energies and excitation energies. In the TWO-FNR calculation, we only used the values listed in Table 1 as the transferred orbital angular momentum l and intrinsic spin s for simplicity, although j allows other combinations through the relationship $j = l \oplus s$. It should be noted that the two final states of ^{7}Be are assumed to be produced by the ^{7}Li(d, n) reaction with two components of j according to an analysis of the reaction in Ref. [24]. Normalization factors are used as adjustable parameters to reproduce absolute values of experimental data. In the ^{7}Li$(d, n)^8$Be case, for which no data are available, we set N to 1.

The reaction channels of the (d, p) transitions, considered in the present study, and their properties are listed in Table 2. To calculate the Q-values, we used one-neutron separation energies S_n for d (2.23 MeV), ^{7}Li (7.25 MeV), ^{8}Li (2.03 MeV), ^{10}Be (6.81 MeV), ^{13}C (4.95 MeV), and ^{14}C (8.18 MeV). For the (d, p) reaction, we used

the two components of j in the DWBA calculation of the following channels according to analyses presented in Refs. [25,26]: the ^{6}Li$(d, p_{0,1})^7$Li, ^{7}Li$(d, p_{0,1})^8$Li, and ^{9}Be$(d, p_{1,5})^{10}$Be channels. The normalization factors were determined such that DWBA results reproduce experimental data, except the fourth channel of the ^{6}Li$(d, p)^7$Li reaction, for which no data are available.

We used an optical potential between d and a target parameterized by Han et al. [27] and that between an emitted nucleon (n or p) and a residual nucleus by Watson et al. [28] Their values were obtained from the Reference Input Parameter Library (RIPL). It should be noted that two geometrical parameters and one potential depth of the potential between d and the target, namely a diffuseness parameter for the real part a_{V}, a radial parameter for the imaginary surface term r_{Wd}, and a strength for the real part V_0, were adjusted in several cases in order to fit the DWBA results to experimental data. The values of a_{V} and r_{Wd} were set to 0.4 and 1.0 fm, respectively, from the first to sixth reaction channels of ^{9}Be$(d, n)^{10}$B listed in Table 1, except the third channel. For the third channel, we only set $a_{\text{V}} = 0.4$ fm, since the adjustment of r_{Wd} was not required to reproduce the angular distribution of the experimental data. In the DWBA calculation of the ^{6}Li$(d, p)^7$Li channels, we set V_0 to twice the original value to reproduce first peaks observed in experimental data of angular differential cross sections (ADXs).

2.3. Concept and algorithm in PHITS

The combined method is based on the idea that the nuclear reaction processes attributed to each model can be distinguished spatially. The "direct process" in DWBA occurs at the surface of the target nucleus, whereas the cascade processes described by INCL generally occur inside the nucleus. Furthermore, the direct process is a coherent process, while the cascade processes are basically incoherent. This is confirmed by the fact that the neutrons issued from the first process generally have a larger energy than the incident energy, whereas a large majority of the neutrons generated by the cascade have an energy smaller than the incident energy, as illustrated by Figs. 16–21 in the next section. Therefore, there is no real interference between the two contributions, and we can obtain the final result of the neutron spectrum by summing two contributions given by the models. It should be noted that the above assumption should be confirmed when the method is used for reactions other than those considered in this paper, because important processes to describe neutron or proton spectra depend on their incident energies and target nuclei.

We use the algorithm shown in Fig. 2 to perform the method in PHITS. When a nuclear reaction occurs in a PHITS simulation, the occurrence of a DWBA event is randomly determined according to the ratio of the DWBA cross section σ_{DWBA} to the total reaction cross section. The σ_{DWBA} is calculated by integrating over emitted angles and summing over reaction channels of ADXs. If the DWBA event occurred, a reaction channel is subsequently selected at random from all possible channels shown in Tables 1 and 2. In the case that the (d,n) reaction is selected, the energies and momenta of an emitted neutron and a residual nucleus are determined from a database of ADXs, prepared in advance by the TWO-FNR code. Then, the emission energy of the neutron is randomly determined according to a Lorentzian distribution centered at the excitation energy E_{ex} with the width Γ except for $\Gamma = 0$, and the emission energy of the residue is calculated to satisfy the energy and momentum conservation law. If the DWBA event does not occur, an INCL calculation is performed to obtain a nuclear reaction event. In principle, the INCL impact parameter distribution should be depleted in the region of very peripheral impact parameters, corresponding to DWBA events. However, since the cross section for
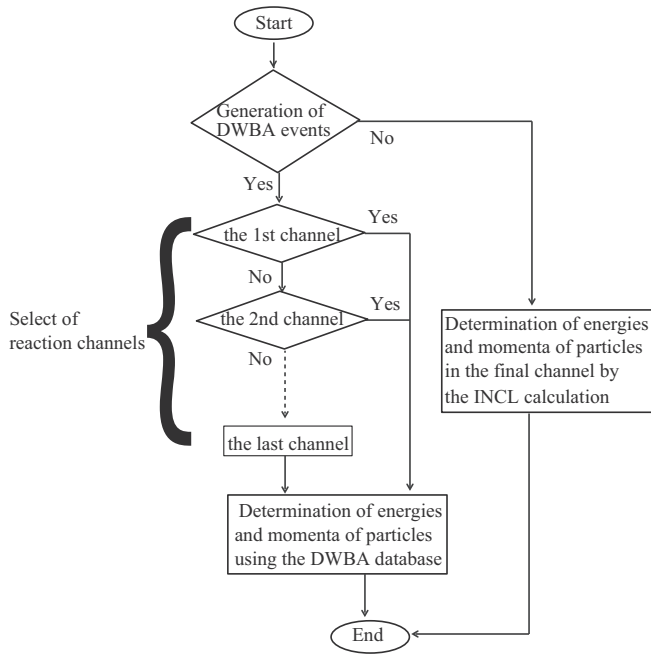
Fig. 2. Flow chart of the algorithm using the combined method.

Table 1
Reaction channels included in the calculation and their properties. Excitation energy E_{ex}, decay width Γ, and Q-value are shown in MeV units. Transferred total angular momentum j, orbital angular momentum l, intrinsic spin s, and normalization factor N are also shown. For the ^{6}Li$(d,n_{0,1})^{7}$Be channels, we used two components of j. The information on $j = l \oplus s$ and N of the second one is given in the next line.

Reaction channels	E_{ex}	Γ	Q-value	$j = l \oplus s$	N
^{6}Li$(d,n_0)^{7}$Be	0(g.s.)	0^{a}	+3.38	$3/2 = 1 \oplus 1/2$	0.31
				$1/2 = 1 \oplus 1/2$	0.20
^{6}Li$(d,n_1)^{7}$Be	0.43	0^{a}	+2.95	$3/2 = 1 \oplus 1/2$	0.60
				$1/2 = 1 \oplus 1/2$	0.028
^{7}Li$(d,n_0)^{8}$Be	0(g.s.)	$6.8e^{-6}$	+15.03	$3/2 = 1 \oplus 1/2$	1
^{7}Li$(d,n_1)^{8}$Be	3.04	1.50	+11.99	$1/2 = 1 \oplus 1/2$	1
^{9}Be$(d,n_0)^{10}$B	0(g.s.)	0	+4.36	$3/2 = 1 \oplus 1/2$	0.60
^{9}Be$(d,n_1)^{10}$B	0.72	0^{a}	+3.64	$1/2 = 1 \oplus 1/2$	0.87
^{9}Be$(d,n_2)^{10}$B	1.74	0^{a}	+2.62	$3/2 = 1 \oplus 1/2$	0.80
^{9}Be$(d,n_3)^{10}$B	2.15	0^{a}	+2.21	$3/2 = 1 \oplus 1/2$	0.45
^{9}Be$(d,n_4)^{10}$B	3.59	0^{a}	+0.77	$1/2 = 1 \oplus 1/2$	0.21
^{9}Be$(d,n_5)^{10}$B	4.77	$7.8e^{-6}$	−0.41	$7/2 = 3 \oplus 1/2$	0.30
^{9}Be$(d,n_6)^{10}$B	5.11	$0.98e^{-3}$	−0.75	$1/2 = 0 \oplus 1/2$	0.39
^{9}Be$(d,n_7)^{10}$B	5.16	$1.8e^{-6}$	−0.80	$3/2 = 1 \oplus 1/2$	0.68
^{9}Be$(d,n_8)^{10}$B	5.92	$5.82e^{-3}$	−1.56	$1/2 = 1 \oplus 1/2$	0.64
^{9}Be$(d,n_9)^{10}$B	6.13	$1.52e^{-3}$	−1.77	$5/2 = 2 \oplus 1/2$	0.59
^{9}Be$(d,n_{10})^{10}$B	6.56	$25.2e^{-3}$	−2.20	$5/2 = 2 \oplus 1/2$	0.44
^{12}C$(d,n_0)^{13}$N	0(g.s.)	0^{a}	−0.28	$1/2 = 1 \oplus 1/2$	1.00
^{13}C$(d,n_0)^{14}$N	0(g.s.)	0	+5.33	$1/2 = 1 \oplus 1/2$	1.00
^{13}C$(d,n_1)^{14}$N	2.31	0^{a}	+3.01	$1/2 = 1 \oplus 1/2$	1.00
^{13}C$(d,n_2)^{14}$N	3.95	0^{a}	+1.38	$1/2 = 1 \oplus 1/2$	1.00

[a] long-lived states.

Table 2
The (d,p) reaction channels included in this study. The meaning of the variables is the same as in Table 1. We used two j components in the calculation for the ^{6}Li$(d,p_{0,1})^{7}$Li, ^{7}Li$(d,p_{0,1})^{8}$Li, and ^{9}Be$(d,p_{1,5})^{10}$Be channels. The information on $j = l \oplus s$ and N for the channels is given in each two lines.

Reaction channels	E_{ex}	Γ	Q-value	$j = l \oplus s$	N
^{6}Li$(d,p_0)^{7}$Li	0(g.s.)	0	+5.03	$3/2 = 1 \oplus 1/2$	0.66
				$1/2 = 1 \oplus 1/2$	0.45
^{6}Li$(d,p_1)^{7}$Li	0.48	0^{a}	+4.55	$3/2 = 1 \oplus 1/2$	0.93
				$1/2 = 1 \oplus 1/2$	0.042
^{6}Li$(d,p_2)^{7}$Li	4.63	$93e^{-3}$	+0.40	$5/2 = 3 \oplus 1/2$	0.42
^{6}Li$(d,p_3)^{7}$Li	6.68	0.88	−1.66	$7/2 = 3 \oplus 1/2$	1
^{7}Li$(d,p_0)^{8}$Li	0(g.s.)	0^{a}	−0.192	$3/2 = 1 \oplus 1/2$	0.95
				$1/2 = 1 \oplus 1/2$	0.054
^{7}Li$(d,p_1)^{8}$Li	0.98	0^{a}	−1.17	$3/2 = 1 \oplus 1/2$	0.81
				$1/2 = 1 \oplus 1/2$	0.31
^{9}Be$(d,p_0)^{10}$Be	0(g.s.)	0^{a}	+4.59	$3/2 = 1 \oplus 1/2$	1.29
^{9}Be$(d,p_1)^{10}$Be	3.37	0^{a}	+1.22	$3/2 = 1 \oplus 1/2$	0.46
				$1/2 = 1 \oplus 1/2$	0.24
^{9}Be$(d,p_2)^{10}$Be	5.958	0^{a}	−1.371	$3/2 = 1 \oplus 1/2$	0.79
^{9}Be$(d,p_3)^{10}$Be	5.960	0^{a}	−1.373	$1/2 = 0 \oplus 1/2$	0.79
^{9}Be$(d,p_4)^{10}$Be	6.18	0^{a}	−1.59	$3/2 = 1 \oplus 1/2$	1.01
^{9}Be$(d,p_5)^{10}$Be	6.26	0^{a}	−1.68	$1/2 = 0 \oplus 1/2$	0.68
				$5/2 = 2 \oplus 1/2$	0.33
^{12}C$(d,p_0)^{13}$C	0(g.s.)	0	+2.72	$1/2 = 1 \oplus 1/2$	0.85
^{12}C$(d,p_1)^{13}$C	3.09	0^{a}	−0.37	$1/2 = 0 \oplus 1/2$	1.12
^{12}C$(d,p_2)^{13}$C	3.69	0^{a}	−0.96	$3/2 = 1 \oplus 1/2$	0.32
^{12}C$(d,p_3)^{13}$C	3.85	0^{a}	−1.13	$5/2 = 2 \oplus 1/2$	1.70
^{13}C$(d,p_0)^{14}$C	0(g.s.)	0^{a}	+5.95	$1/2 = 1 \oplus 1/2$	1.24
^{13}C$(d,p_1)^{14}$C	6.09	0^{a}	−0.14	$1/2 = 0 \oplus 1/2$	0.73
^{13}C$(d,p_2)^{14}$C	6.59	0^{a}	−0.64	$1/2 = 1 \oplus 1/2$	0.28
^{13}C$(d,p_3)^{14}$C	6.73	0^{a}	−0.78	$5/2 = 2 \oplus 1/2$	0.71
^{13}C$(d,p_4)^{14}$C	6.90	0^{a}	−0.95	$1/2 = 0 \oplus 1/2$	0.96
^{13}C$(d,p_5)^{14}$C	7.01	0^{a}	−1.06	$3/2 = 1 \oplus 1/2$	0.13
^{13}C$(d,p_6)^{14}$C	7.34	0^{a}	−1.39	$5/2 = 2 \oplus 1/2$	0.70

^{nat}Li and ^{nat}C targets with deuteron energies of 40 MeV and for the ^{9}Be target with energies of 10 and 18 MeV.
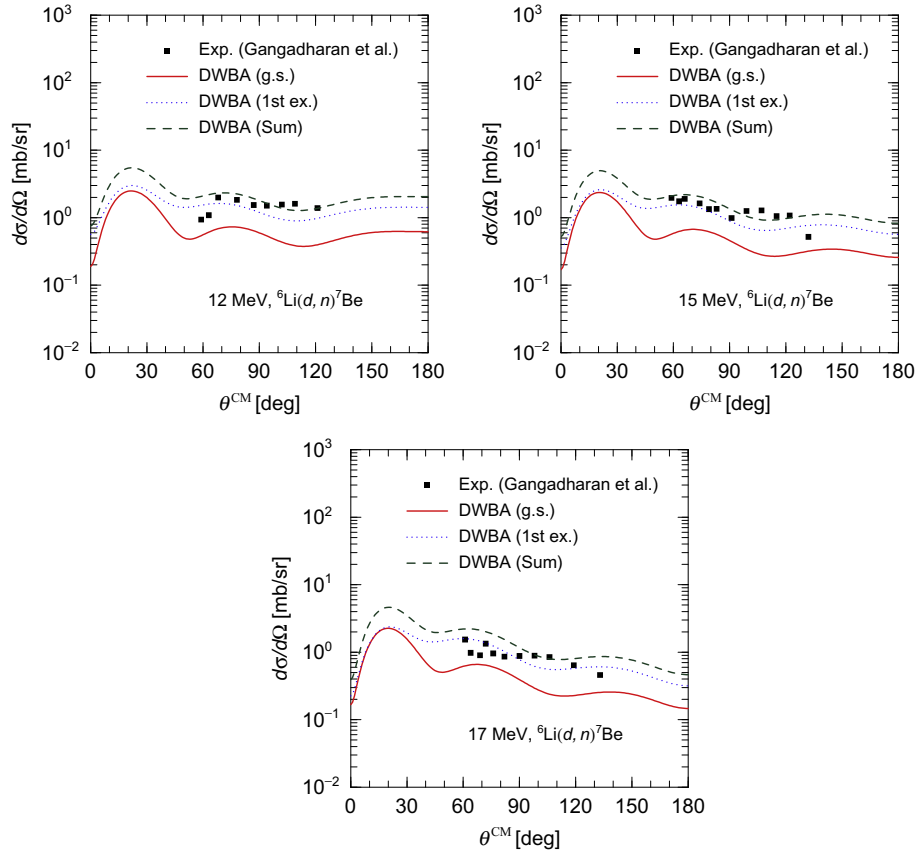
3. Results and discussion

3.1. (d,n) and (d,p) cross sections obtained by DWBA

For an accurate description of the (d,n) and (d,p) reactions, we used the normalization factor N as an adjustable parameter so that ADXs, obtained by DWBA, reproduce experimental data within the energy range of interest, except for several channels for which no data are available. For these channels, ^{7}Li$(d,n_{0,1})^{8}$Be and ^{6}Li$(d,p_3)^{7}$Li, we assumed N to be 1, as shown in Tables 1 and 2. We present here comparisons of ADXs obtained by DWBA with experimental data. The ADX database contains results of calculations performed in the energy regions of interest.

3.1.1. (d,n) reactions on ^{6,7}Li targets
Fig. 3 shows ADXs of the ^{6}Li$(d,n)^{7}$Be reaction at incident energies of 12, 15, and 17 MeV. Solid and dotted lines correspond to ADXs calculated with two final states of ^{7}Be: the ground and the first excited states, respectively. For this reaction system, we assumed that the two transitions have two components, $j = 3/2$ and 1/2, as shown in Table 1, according to the analysis by Gangadharan and Wolke [24]. Therefore, we had to determine a total of four normalization factors. However, since the available experimental data [24] include only the sum of contributions of the two transitions, we adopted spectroscopic factors for the components S, obtained in Ref. [29], as the basic values, and determined a

cascade events is considerably larger than that for the DWBA events, this approximation is largely harmless.

We created a database of ADXs in (d,n) and (d,p) reactions on ^{6,7}Li and ^{12,13}C targets for deuteron incident energies from 10 to 50 MeV and of those on the ^{9}Be target for energies from 5 to 25 MeV. As will be shown in the next section, these energy ranges are necessary for analyzing inclusive (d,xn) and (d,xp) spectra for

Fig. 3. Angular differential cross sections (ADXs) of the ^{6}Li$(d,n)^7$Be reaction for incident energies of 12 (upper-left panel), 15 (upper-right panel), and 17 MeV (lower panel). Experimental data [24] are denoted by closed squares. ADXs producing ^{7}Be ground and first excited states, calculated by Distorted Wave Born Approximation (DWBA), are represented by solid and dotted lines, respectively. Dashed lines represent the sum of two contributions.

coefficient C multiplied to all values, which allowed comparison of the absolute values of the data. The spectroscopic factors we used are listed in Table 3. The coefficient was set to 0.71 so that the DWBA result reproduces the experimental data. Results of the multiplication $N = CS$ are given in Table 1.

In Fig. 3, the calculated results of the summation are denoted by dashed lines. Cross sections of two transitions are similar to each other for first peaks at 20°. At angles greater than 30°, cross sections for the transition to the first excited state are dominant contributors to the sums. Although experimental data [24], represented by closed squares, are limited only at the region between 60° and 140°, results calculated by DWBA successfully reproduce the data.

For the ^{7}Li target, normalization factors N were assumed to be 1 because of deficiencies in the available data. Therefore, there is uncertainty in their absolute values.

3.1.2. (d,n) reactions on ^{9}Be target

ADXs of the reaction ^{9}Be$(d,n)^{10}$B at 7 MeV are shown in Fig. 4. In the present study, 11 final states listed in Table 1, below the proton threshold energy of ^{10}B, are considered. The calculated results for
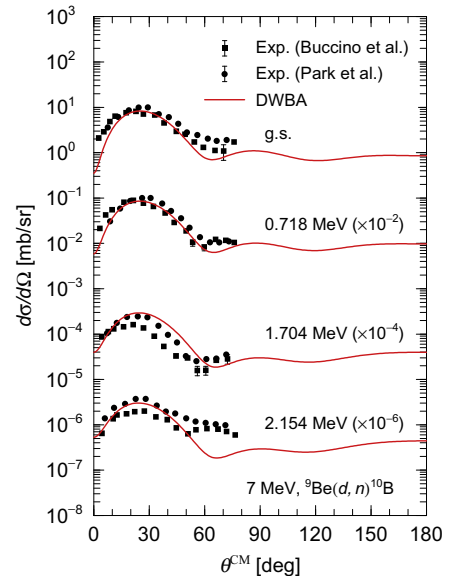
**Fig. 4.** ADXs of ^{9}Be$(d,n)^{10}$B at 7 MeV. The calculated results for four ^{10}B final states are denoted by solid lines. The experimental data of Refs. [30,31] are represented by closed squares and circles, respectively.

lower four states are represented by solid lines in Fig. 4. The results are compared with experimental data [30,31] denoted by closed squares and circles. In addition to normalization factors N, we adjusted two geometrical parameters, a_V and r_{Wd}, of the optical potential between d and ^{9}Be for several channels such that the

Table 3
Spectroscopic factors S for the ^{6}Li$(d,n_{0,1})^7$Be reactions taken from Ref. [29].

Reaction channels	E_{ex}[MeV]	$j = l \oplus s$	S
^{6}Li$(d,n_0)^7$Be	0(g.s.)	$3/2 = 1 \oplus 1/2$	0.43
		$1/2 = 1 \oplus 1/2$	0.29
^{6}Li$(d,n_1)^7$Be	0.43	$3/2 = 1 \oplus 1/2$	0.85
		$1/2 = 1 \oplus 1/2$	0.039
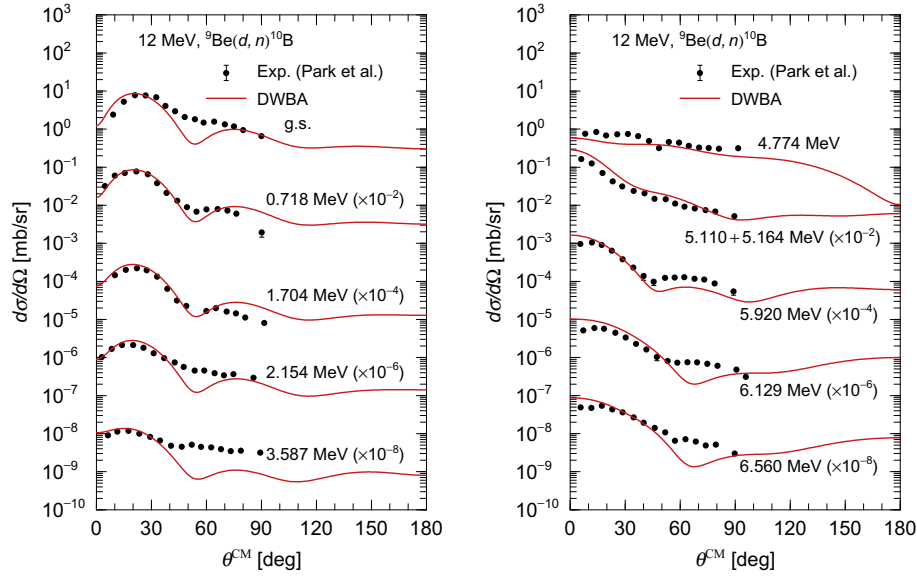
Fig. 5. ADXs of the ^{9}Be$(d,n)^{10}$B reaction for 12 MeV. By using solid lines, calculated results for five and six ^{10}B final states are shown in left and right panels, respectively. Experimental data denoted by closed circles are taken from Ref. [31]. The second line from the top in the right panel represents the sum of two results for ^{10}B final states with E_{ex} = 5.110 and 5.164 MeV.

DWBA results reproduce absolute values and shapes of peaks at ~30° in the data.

Fig. 5 shows ADXs of ^{9}Be$(d,n)^{10}$B at 12 MeV for the 11 states. For E_{ex} = 5.110 and 5.164 MeV, we show only the sum of their contributions corresponding to the experimental data [31]. The calculated ADXs (solid lines) reproduce the experimental data (closed circles), similar to Fig. 4. Although there are small deviations between calculated results and data at ~60° for some channels, these can be attributed to another component of j or l. To improve the calculation by considering some other components, a more detailed analysis of the ^{10}B structure is required. For simplicity, therefore, we considered only one component in this reaction.

Fig. 6 shows results of the reaction at 15 MeV for all states, except E_{ex} = 4.774 MeV. The experimental data from Ref. [31] are denoted by closed circles, and are available for forward to

backward angles. The calculated results represented by solid lines agree with the experimental data, except for the deviations at ~60°. It should be noted that the deviations are smaller than those for 12 MeV shown in Fig. 5.

3.1.3. (d,n) reactions on ^{12,13}C targets

ADXs for the ^{12}C$(d,n)^{13}$N reaction at deuteron incident energies of 12 and 13 MeV are shown in the left and right panels of Fig. 7, respectively. The closed squares and circles in the left panel denote the experimental data from Refs. [24,32], respectively, and the closed circles in the right panel represent those from Ref. [33]. Although we set N = 1.00, as shown in Table 1, the results calculated by DWBA (solid lines) reproduce the data at the whole angle in both panels. The interference patterns of the DWBA results also agree with those of the data.
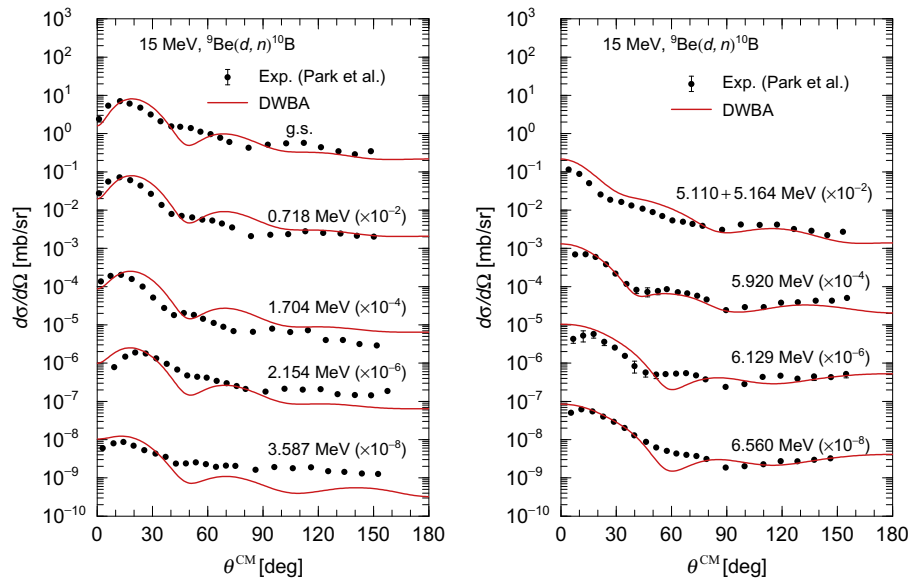
Fig. 6. ADXs of ^{9}Be$(d,n)^{10}$B for 15 MeV. The experimental data [31] are represented by closed circles, and the results obtained by DWBA are denoted by solid lines. The result for E_{ex} = 4.774 MeV is not shown as experimental data are not available.
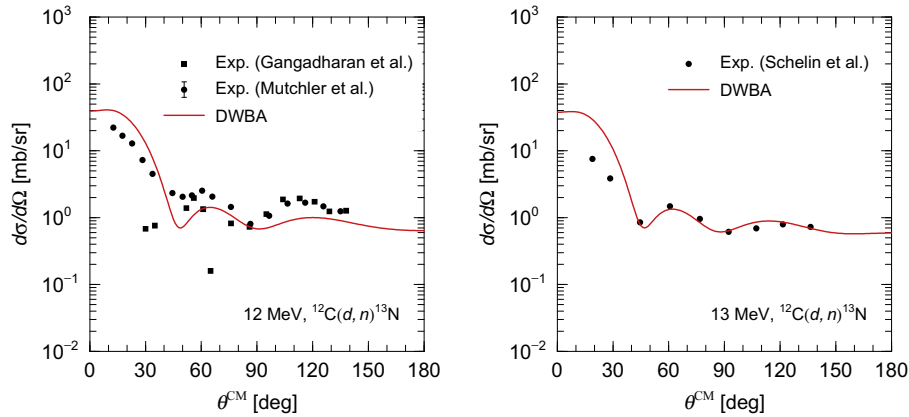
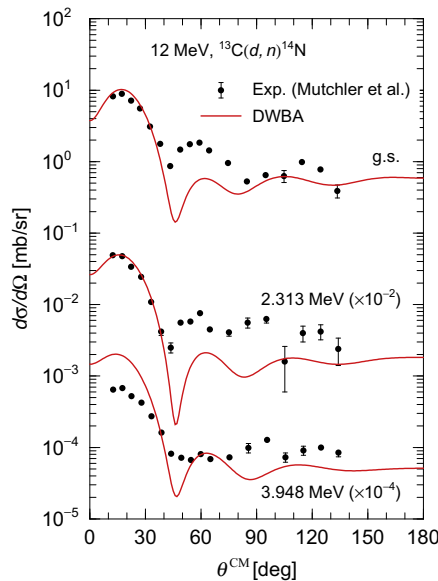**Fig. 7.** ADXs of the ^{12}C$(d,n)^{13}$N reaction at 12 (left panel) and 13 MeV (right panel). The results of DWBA, represented by solid lines, are compared with experimental data, denoted by symbols. The data in the left panel are taken from Refs. [24,32], and those in the right panel are from Ref. [33].

Fig. 8 shows differential cross sections of ^{13}C$(d,n)^{14}$N at 12 MeV. The three solid lines correspond to DWBA results for each of the final states of ^{14}N listed in Table 1, and the closed circles represent the experimental data taken from Ref. [32]. In this reaction, normalization factors N were also set to 1.00, since the results calculated with this value reproduce data effectively for first peaks at 20°. The reasonable agreement between the DWBA results and experimental data is found in other angles, except at ∼50°. Small deviations at this angle can be attributed to the omission of another j or l component. As in the ^{9}Be case, detailed analyses of ground and excited states of ^{14}N are required to improve the DWBA calculation.

3.1.4. (d,p) reactions on ^{6,7}Li targets

Fig. 9 shows ADXs of the ^{6}Li$(d,p)^7$Li reaction at 12 MeV for the ground and the first excited states of ^{7}Li. As in the case of the ^{6}Li$(d,n)^7$Be reaction, we assumed these (d,p) transitions have two components of $j = 3/2$ and $1/2$ shown in Table 2, according to the analysis by Schiffer et al. [25]. The normalization factors shown in Table 2 are results of the multiplication $N = CS$. The spectroscopic factors S, we used as the basic values, are listed in Table 4.

We set the coefficients C to 1.5 and 1.1 for the transitions to the ^{7}Li ground and excited states, respectively. These values of C were determined so that the DWBA results reproduce absolute values of peaks at ∼20° in the experimental data. In addition to C, we set the strength for the real part of the optical potential between d and ^{6}Li, V_0, to twice the original value in order to reproduce shapes of the peaks. The peaks of the calculated results agree well with those of the data by the adjustment of C and V_0. However, there are small deviations between the calculated results and the data at angles greater than 50°. Although we performed the DWBA calculation with the two components of j, detailed analyses considering some other components are required to reproduce the data more precisely.
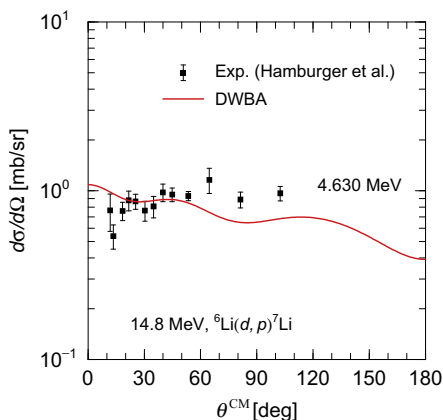
ADXs of the ^{6}Li$(d,p)^7$Li reaction at 14.8 MeV for the second excited state of ^{7}Li are shown in Fig. 10. In the DWBA calculation for this reaction channel, we also adopted the same adjustment of V_0 as in the previous two channels of ^{6}Li$(d,p)^7$Li. The normalization factor was determined such that the DWBA result agrees with the experimental data at ∼20°. The calculated result is found to be in good agreement with the data at angles smaller than 50°, although there is a small deviation at the region between 60° and 110°.

Fig. 8. ADXs of ^{13}C$(d,n)^{14}$N for 12 MeV. The calculated results, denoted by solid lines, are compared with experimental data [32], represented by closed circles. Results for three ^{14}N final states, listed in Table 1, are shown.
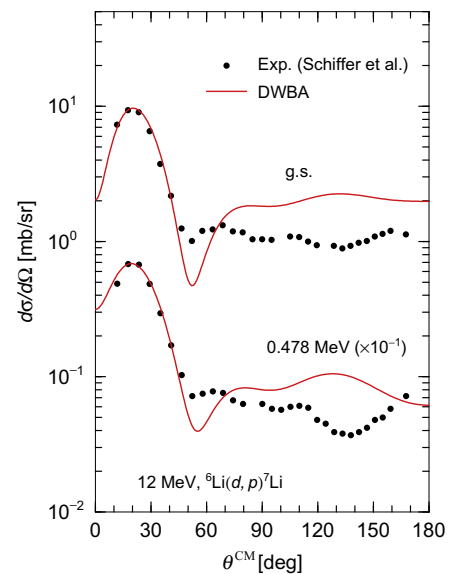
Fig. 9. ADXs of the ^{6}Li$(d,p)^7$Li reaction for an incident energy of 12 MeV. Solid lines represent the DWBA results for the transitions to the ground and first excited states of ^{7}Li. Experimental data [25] are denoted by closed circles.

Table 4
Spectroscopic factors S for the ^{6}Li$(d,p_{0,1})^7$Li and ^{7}Li$(d,p_{0,1})^8$Li reactions obtained from Ref. [29].

Reaction channels	E_{ex}[MeV]	$j = l \oplus s$	S
^{6}Li$(d,p_0)^7$Li	0(g.s.)	$3/2 = 1 \oplus 1/2$	0.43
		$1/2 = 1 \oplus 1/2$	0.29
^{6}Li$(d,p_1)^7$Li	0.48	$3/2 = 1 \oplus 1/2$	0.86
		$1/2 = 1 \oplus 1/2$	0.039
^{7}Li$(d,p_0)^8$Li	0(g.s.)	$3/2 = 1 \oplus 1/2$	0.98
		$1/2 = 1 \oplus 1/2$	0.056
^{7}Li$(d,p_1)^8$Li	0.98	$3/2 = 1 \oplus 1/2$	0.32
		$1/2 = 1 \oplus 1/2$	0.12

Fig. 10. ADXs of the ^{6}Li$(d,p)^7$Li reaction at 14.8 MeV for the transition to the second excited state of ^{7}Li. The DWBA result (solid line) and experimental data (closed squares) obtained from Ref. [34] are shown.

For the fourth reaction channel of ^{6}Li$(d,p)^7$Li listed in Table 2, the normalization factors N was assumed to be 1 as experimental data are not available. We used the same adjustment of V_0 as in the other ^{6}Li$(d,p)^7$Li reactions, for the consistency of the DWBA calculation among these reaction channels. Therefore, there is uncertainty in the calculated result. Experimental data are desirable to reduce the uncertainty.

Fig. 11 shows ADXs of ^{7}Li$(d,p)^8$Li at 12 MeV for the ground and the first excited states of ^{8}Li. According to the analysis presented in Ref. [25], we also assumed these (d,p) transitions have two components of $j = 3/2$ and $1/2$ shown in Table 2. The spectroscopic factors S for the components are listed in Table 4. We set the coefficients C to 0.97 (the ground state) and 2.5 (the first excited state), which are determined so that the DWBA results reproduce the data at the region between 10° and 20°. The reasonable agreement between the calculated results and the data is found in Fig. 11, except for small deviations at angles greater than 50°.

3.1.5. (d,p) reactions on ^{9}Be target

Fig. 12 shows ADXs of the ^{9}Be$(d,p)^{10}$Be reaction at 15 MeV for the six final states listed in Table 2. The third and fourth results from the top represent the sum of two results for the final states of ^{10}Be. The third result is the sum of the DWBA results with E_{ex} = 5.958 and 5.960 MeV (the second and third excited states, respectively), and the fourth one is that with E_{ex} = 6.179 and 6.263 MeV (the fourth and fifth excited states, respectively). We assumed the (d,p) transitions to the first and fifth excited states of ^{10}Be have two components of j, according to the analysis by Darden et al. [26]. Their spectroscopic factors S and j are listed in Table 5. The normalization factors shown in Table 2 were determined so that the calculated results agree with the data at ~15°.
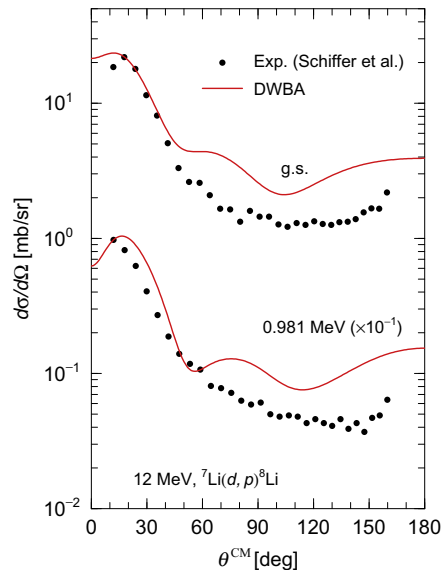
Fig. 11. ADXs of the ^{7}Li$(d,p)^8$Li reaction for 12 MeV. The results of of DWBA for the transitions to the ^{8}Li ground and first excited states are represented by solid lines. Experimental data obtained from Ref. [25] are denoted by closed circles.

It should be noted that we determined the coefficient C and then obtained the normalization factor as the result of the multiplication $N = CS$ for the two transitions having two components of j.

The DWBA result for the ^{10}Be ground state, represented by the first solid line from the top in Fig. 12, sufficiently reproduces the experimental data, except for a deviation at ~45°. The calculated result for the first excited state also underestimates the data at ~45°. These deviations can be attributed to the omission of another j or l component. For the transition to the first excited state, there is a deviation between the DWBA result and the data at angles greater than 90°. To reduce the deviations, detailed analyses of the two states of ^{10}Be are required. On the other hand, both the
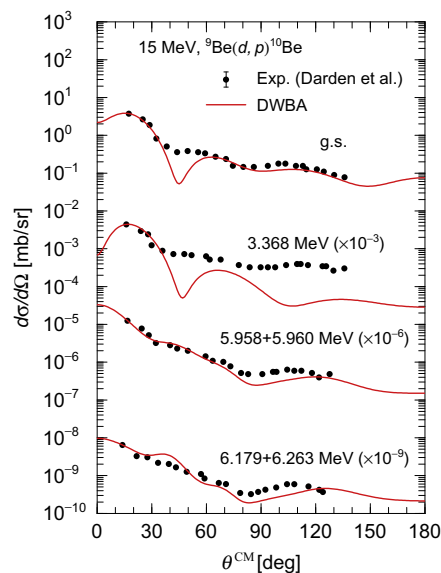
Fig. 12. ADXs of ^{9}Be$(d,p)^{10}$Be at 15 MeV. The DWBA results for six final states of ^{10}Be are shown by solid lines. The third and fourth lines from the top represent the sum of two results for the ^{10}Be final states. The third line corresponds to the sum of the DWBA results with E_{ex} = 5.958 and 5.960 MeV, and the fourth line represents that with E_{ex} = 6.179 and 6.263 MeV. Experimental data denoted by closed circles are taken from Ref. [26].

Table 5
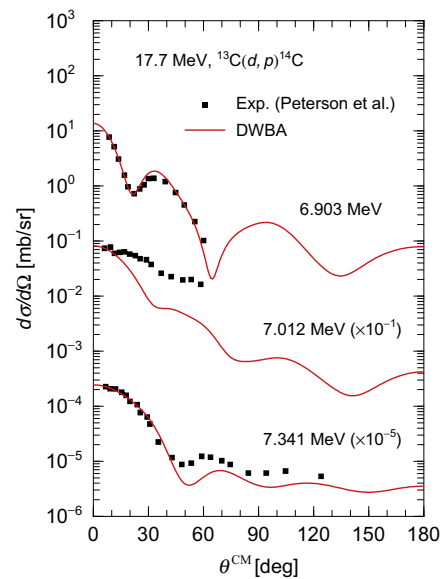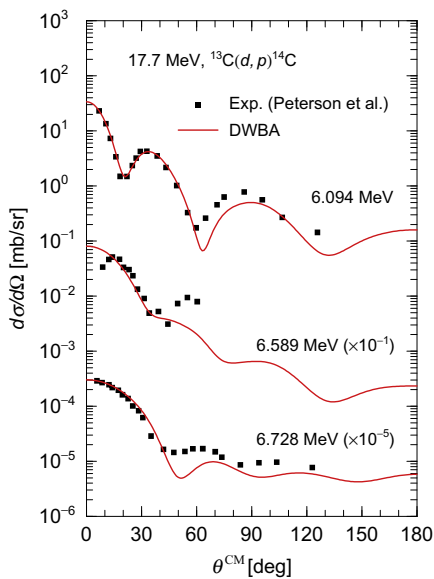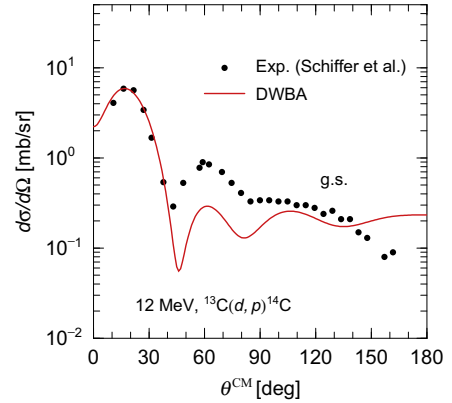Spectroscopic factors S for the ^{9}Be$(d, p_{1.5})^{10}$Be reactions taken from Ref. [26].

Reaction channels	E_{ex}[MeV]	$j = l \oplus s$	S
^{9}Be$(d, p_1)^{10}$Be	3.37	$3/2 = 1 \oplus 1/2$	0.23
		$1/2 = 1 \oplus 1/2$	0.12
^{9}Be$(d, p_5)^{10}$Be	6.26	$1/2 = 0 \oplus 1/2$	0.13
		$5/2 = 2 \oplus 1/2$	0.065
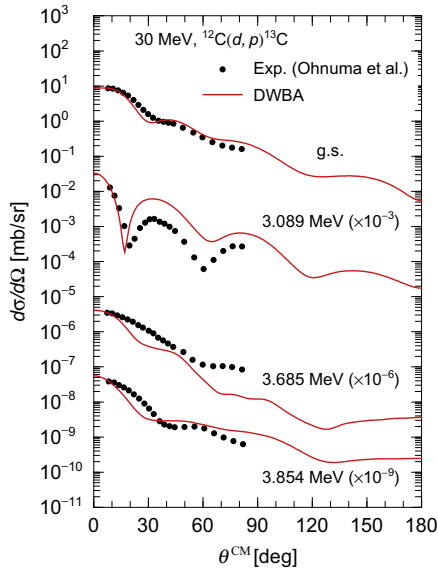
Fig. 13. ADXs of the ^{12}C$(d, p)^{13}$C reaction for 30 MeV. Solid lines represent the calculated results for four ^{13}C final states. Closed circles denote experimental data [35].

third and fourth lines from the top in Fig. 12 successfully agree with the experimental data at the whole angle.
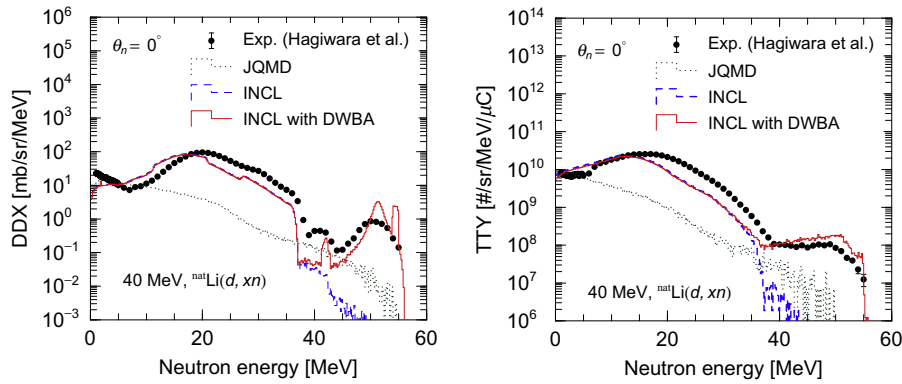
3.1.6. (d, p) reactions on ^{12,13}C targets

ADXs of ^{12}C$(d, p)^{13}$C at 30 MeV for the four final states of ^{13}C are shown in Fig. 13. The normalization factors were determined such that the calculated results agree with the data at ∼8°. The

Fig. 14. ADXs of ^{13}C$(d, p)^{14}$C at 12 MeV. The calculated result for the transition to ground state of ^{14}C is denoted by a solid line. Experimental data [25] are represented by closed circles.

reasonable agreement between the results calculated by DWBA and the measured data is found, although the DWBA result with E_{ex} = 3.089 MeV sightly overestimates the corresponding data at angles greater than 20°. It should be noted that the interference pattern of the second line from the top in Fig. 13 agrees with that of the measured data.

Fig. 14 shows ADXs of the ^{13}C$(d, p)^{14}$C reaction at 12 MeV for the ^{14}C ground state. The normalization factor was determined so that an absolute value of a peak at ∼20° in the measured data agrees with that of the DWBA result. The calculated result successfully reproduces the shape of the peak of the data. Although the DWBA result slightly underestimates the data at the region between 40° and 100°, the overall agreement of the result with the data is reasonable.

Fig. 15 shows ADXs of ^{13}C$(d, p)^{14}$C at 17.7 MeV for the first, second, and third excited states (left panel), and the fourth, fifth, and sixth excited states (right panel). In the DWBA calculation, the normalization factors N were determined so that the DWBA results reproduce the data at the smallest angle, except the transition to the second excited state with E_{ex} = 6.589 MeV. In the case of E_{ex} = 6.589 MeV, we set N such that the calculated result agrees with an absolute value of a peak at ∼15° in the data. Although a

Fig. 15. ADXs of the ^{13}C$(d, p)^{14}$C reaction at 17.7 MeV for six excited states of ^{14}C. The DWBA results are represented by solid lines, and experimental data obtained from Ref. [36] are denoted by closed squares.

Fig. 16. Double differential cross sections (DDXs) (left panel) and thick target neutron yields (TTYs) (right panel) at the neutron emission angle $\theta_n = 0°$ in $^{nat}Li(d,xn)$ for 40 MeV. Experimental data taken from Ref. [38] are denoted by closed circles, and calculated results obtained by JAERI Quantum Molecular Dynamics (JQMD), only Intra-Nuclear Cascade of Liège (INCL), and INCL with DWBA are represented by dotted, dashed, and solid lines, respectively.

deviation between the DWBA result and the data in the reaction with E_{ex} = 7.012 MeV, the results are found to be in good agreement with the data. To reduce the deviation, detailed analyses of the excited state of ^{14}C are required.

### 3.2. Inclusive (d,xn) and (d,xp) spectra obtained by PHITS with new method

In general, inclusive (d,xn) spectra for the incident energies considered here consist mainly of discrete peaks around the same neutron energy as the incident deuteron and broad peaks lying at half the incident energy. We will discuss neutron spectra for both thin and thick targets and compare the results obtained by the new method with experimental data. The shape of the discrete peak for the thin target is very different from that for the thick target since various reactions resulting from the incident deuteron losing its energy through the thick material contribute to the spectrum in the latter case. In contrast, the shapes of broad peaks for both thin and thick targets are relatively similar.

Inclusive (d,xp) spectra have similar features to the (d,xn) spectra. Experimental data of $^9Be(d,xp)$ and $^{12}C(d,xp)$ spectra at forward angles for the 100-MeV incident energy, which were

measured by Ridikas et al. [37], exhibit broad peaks at the emitted proton of 50 MeV and discrete peaks around 100 MeV. Ye et al. analyzed the experimental data, and verified that the stripping process is the dominant contributor to the broad peak as in the (d,xn) spectra [15]. Therefore, INCL considering the process is expected to reproduce the broad peak. By combining INCL and DWBA, the new method can describe both the broad peaks and discrete peaks in the proton spectra. Because experimental data of the (d,xp) spectrum for the incident energy below 50 MeV are not available, we will show the comparison between calculated results to discuss the validity of the method for the proton spectra.

3.2.1. (d,xn) spectra on ^{nat}Li targets

DDXs and thick target neutron yields (TTYs) at the 0° neutron emission angle in the $^{nat}Li(d,xn)$ reaction for the 40-MeV incident energy are shown in the left and right panels of Fig. 16, respectively. The experimental data [38] are represented by closed circles. DDXs were calculated by PHITS using targets of 0.86 mm thickness, and TTYs were calculated using targets of 21.4 mm thickness. Results obtained by the PHITS calculation using three types of nuclear reaction models, JQMD, INCL, and the combined method (INCL with DWBA), are denoted by dotted, dashed, and
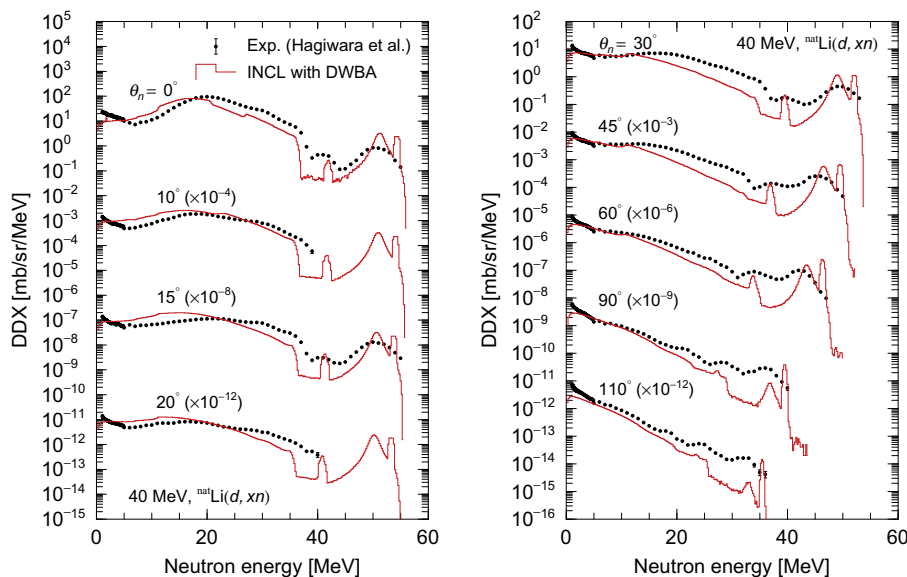
Fig. 17. DDXs in the $^{nat}Li(d,xn)$ reaction for 40 MeV at $\theta_n = 0°, 10°, 15°,$ and $20°$ (left panel) and $\theta_n = 30°, 45°, 60°, 90°,$ and $110°$ (right panel). Results of INCL with DWBA denoted by solid lines are compared with experimental data [38] represented by closed circles.
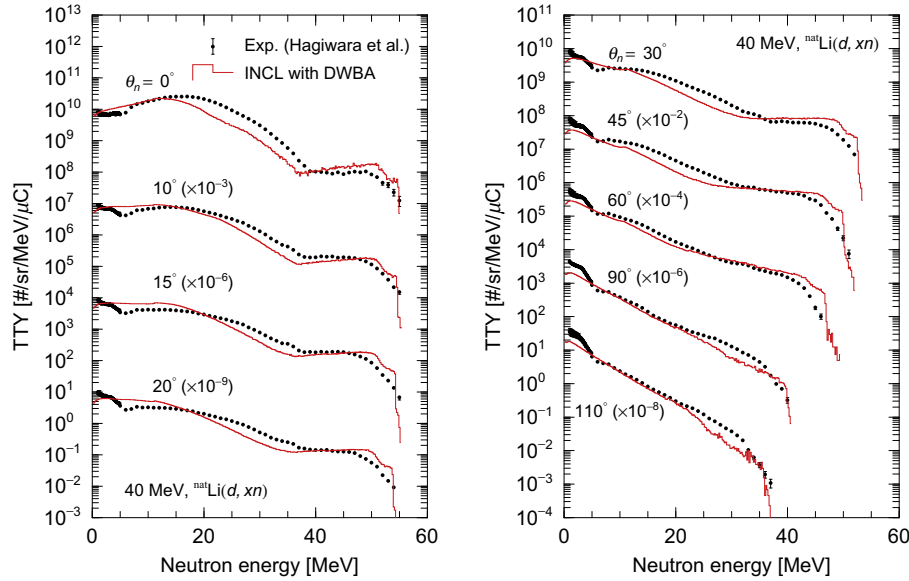
Fig. 18. TTYs in ^{nat}Li(d, xn) for 40 MeV at $\theta_n = 0°, 10°, 15°$, and $20°$ (left panel) and $\theta_n = 30°, 45°, 60°, 90°$, and $110°$ (right panel). Results of INCL with DWBA and experimental data [38] are denoted by solid lines and closed circles, respectively.

solid lines, respectively. Data in the left panel exhibit three peaks around neutron energies of 20, 40, and 50 MeV, except for one at low energies below 5 MeV. Although none of these peaks can be reproduced by JQMD, the left peak is described by the INCL contribution, and the other two peaks are represented by the addition of DWBA. DWBA peaks are very sharp since the calculation used a high energy resolution of 0.2 MeV, unlike the experimental conditions of Ref. [38]. Since reactions on ^{7}Li have higher Q-values than those on ^{6}Li, the right and middle peaks consist of discrete spectra corresponding to transitions of ^{7}Li and ^{6}Li targets, respectively. In contrast, experimental data for TTYs in the right panel exhibit two broad peaks at $\sim$20 and $\sim$50 MeV. The contribution of INCL reproduces the peak on the left side, and that of DWBA describes the peak on the right side. Although the discrete spectra on DDXs can be distinguished from each other, those on TTYs combine into a broad one.

Figs. 17 and 18 show the angular dependence of DDXs and TTYs, respectively, in the same reaction as that shown in Fig. 16. Solid lines represent results obtained by the new method, and closed circles represent experimental data [38] for comparison. Results at emission angles of 0°, 10°, 15°, and 20° are shown in the left panels of Figs. 17 and 18, and those at angles of 30°, 45°, 60°, 90°, and 110° are shown in the two right panels. Experimental data of DDXs show that spectra at angles greater than 60° have small peaks that

can be attributed to transitions between discrete states. Therefore, the new method is very useful for describing neutron spectra at forward angles as well as backward angles although the calculated results slightly underestimate the data at greater angles. Fig. 18 shows that the PHITS calculation with the method is also sufficient to reproduce TTY data.

The DWBA cross sections include the uncertainty associated with energy dependence of the normalization factors. The factors for the ^{6}Li$(d, n)^7$Be reactions were determined so that the DWBA results reproduce the experimental data at incident energies of 12, 15, and 17 MeV. However, the peaks obtained by PHITS, which correspond to the results of ^{6}Li$(d, n)^7$Be, underestimate those of the data at 40 MeV by a factor of 2 or 3, as shown in Fig. 17. Although this result suggests the normalization factors used in the DWBA calculation should depend on the incident energy, we assumed the factors to be constant in the present study, because there are not enough experimental data for the (d, n) and (d, p) reactions to investigate its dependence.

3.2.2. (d, xn) spectra on ^{9}Be targets

Fig. 19 shows DDXs (left panel) and TTYs (right panel) at an emission angle of 3.5° in the deuteron-induced reaction on the ^{9}Be target for an incident energy of 18 MeV. Closed circles represent experimental data taken from Ref. [39], and dotted, dashed,
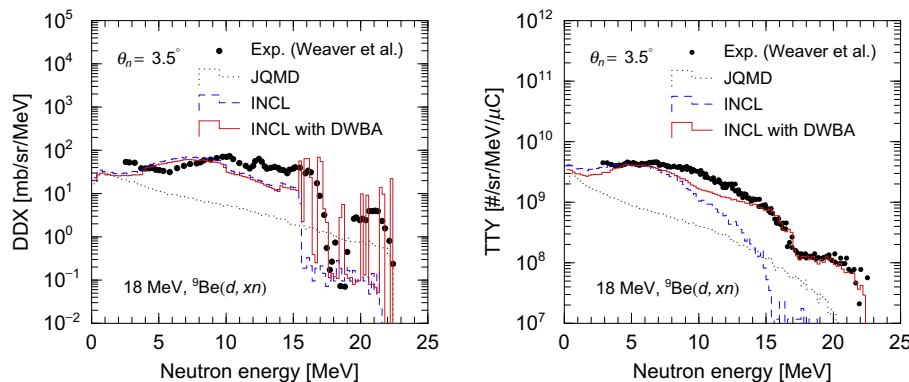
Fig. 19. DDXs (left panel) and TTYs (right panel) at $\theta_n = 3.5°$ in ^{9}Be(d, xn) for 18 MeV. Experimental data [39] are represented by closed circles, and results calculated by Particle and Heavy Ion Transport code System (PHITS) with JQMD, INCL, and INCL with DWBA are denoted by dotted, dashed, and solid lines, respectively.
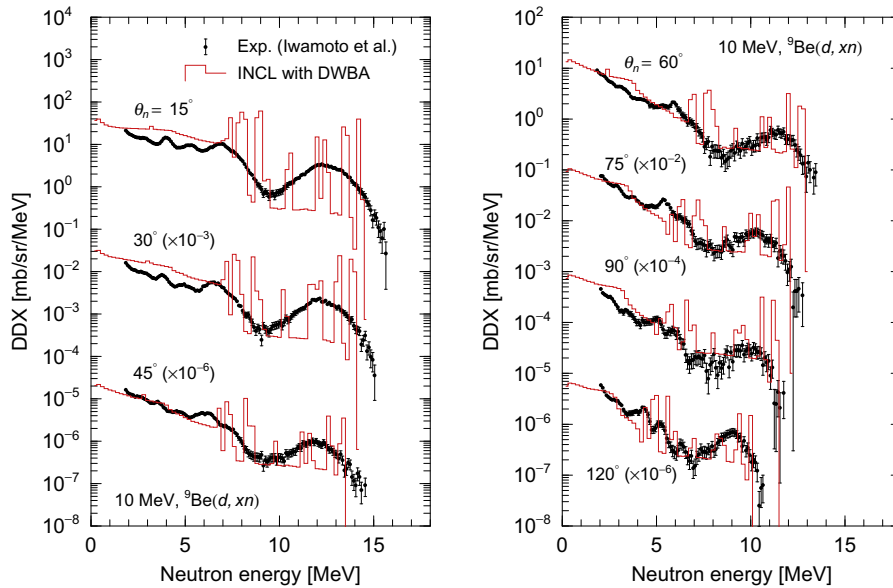
Fig. 20. DDXs in the ^{9}Be(d,xn) reaction for 10 MeV at $\theta_n = 15°$, 30°, and 45° (left panel) and $\theta_n = 60°$, 75°, 90°, and 120° (right panel). Results obtained by INCL with DWBA are represented by solid lines, and experimental data taken from Ref. [40] are denoted by closed circles.

and solid lines denote calculated results of PHITS with JQMD, only INCL, and INCL with DWBA, respectively. In the PHITS calculation, we set the thickness of ^{9}Be to 0.015 mm for the thin target and to 2.5 mm for the thick target. Experimental DDXs show a characteristic structure, which can be attributed to discrete peaks. Only INCL does not sufficiently reproduce the peak at ~20 MeV or below 18 MeV, whereas the new method describes these peaks effectively. In this study, the 11 final states of ^{10}B below the proton threshold energy are considered in DWBA. Discrete spectra of transitions to the states contribute to the two broad peaks. A small discrepancy below 15 MeV is observed possibly because transitions to some states above the threshold were neglected. For reproducing the data more precisely, the improvement of the TWO-FNR code is necessary for such continuum states. For TTYs, the result calculated by PHITS using INCL with DWBA agrees with the data effectively, except for a small deviation at ~10 MeV. The calculation using INCL only is not adequate, and that using JQMD also underestimates the data over the entire range of emitted neutron energies.

Angular dependence of DDXs for the ^{9}Be target in the (d,xn) reaction with the 10-MeV incident energy is shown in Fig. 20. Solid lines represent results calculated by INCL with DWBA, and closed circles denote experimental data [40] measured with a thin target

of 0.015 mm. DDXs at emission angles of 15°, 30°, and 45° are shown in the left panel, and those at angles of 60°, 75°, 90°, and 120° are shown in the right panel. These data trends, composed of the broad peak at the highest neutron energy and the other peaks at lower energies in the spectra, are consistent with those of Ref. [39]. The peaks correspond to the discrete peaks observed in the calculated results, as mentioned in Ref. [40], and can be reproduced by the new method at all angles shown in Fig. 20. Therefore, discrete peaks obtained by DWBA are important for describing neutron spectra at high angles, as in the case of the Li target.

3.2.3. (d,xn) spectra on ^{nat}C targets

In Fig. 21, DDXs at an emission angle of 0° in the ^{nat}C(d,xn) reaction for 40-MeV incident energy are shown in the left panel, and TTYs are shown in the right panel. Dotted, dashed, and solid lines denote calculated results by PHITS using JQMD, INCL, and INCL with DWBA, respectively. The thickness of the target for DDXs in the calculation is set to 0.1 mm, and that for TTYs is set to 6 mm. Experimental data taken from Ref. [9] are represented by closed circles in the right panel only, as DDX data are not available. Four discrete peaks obtained by DWBA in DDX correspond to each transition for ^{12}C and ^{13}C targets listed in Table 1. Except for a feature
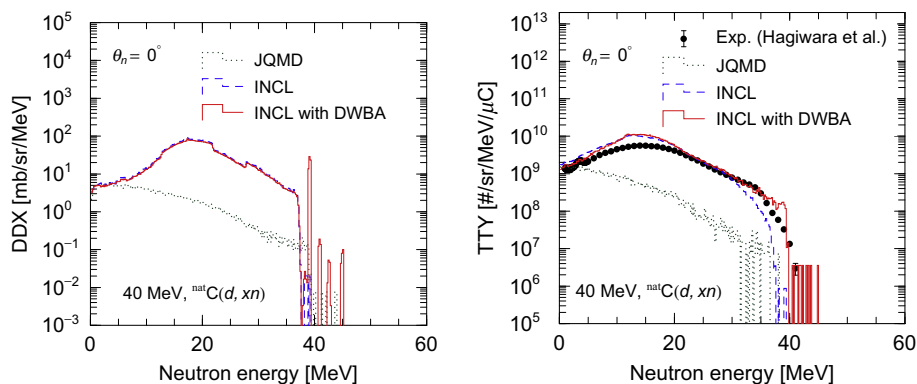
Fig. 21. DDXs (left panel) and TTYs (right panel) at $\theta_n = 0°$ in the ^{nat}C(d,xn) reaction for 40 MeV. Results obtained by JQMD, INCL, and INCL with DWBA are represented by dotted, dashed, and solid lines, respectively. Closed circles in the right panel denote experimental data [9].
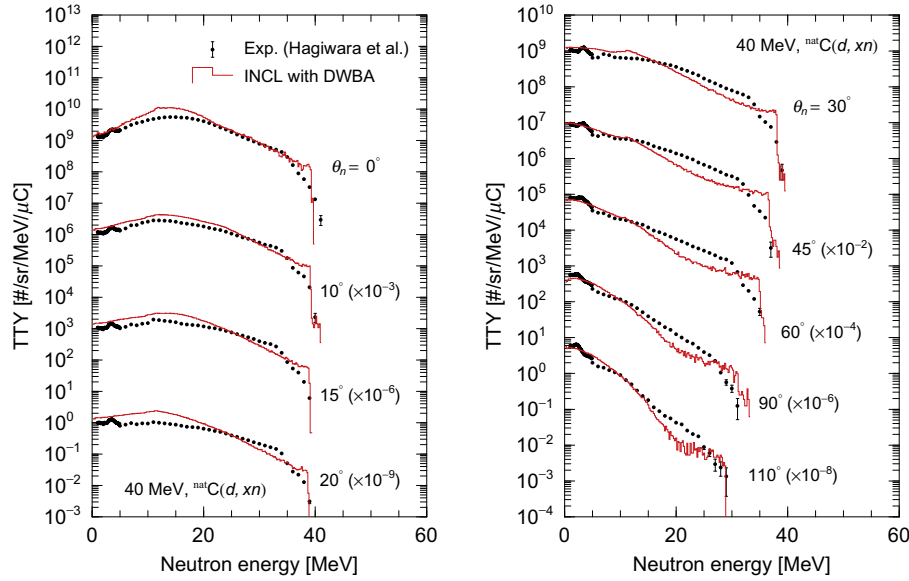
Fig. 22. TTYs in $^{nat}C(d,xn)$ for 40 MeV at $\theta_n = 0°, 10°, 15°,$ and $20°$ (left panel) and $\theta_n = 30°, 45°, 60°, 90°,$ and $110°$ (right panel). Experimental data taken from Ref. [9] are represented by closed circles, and calculated results of INCL with DWBA are denoted by solid lines.

of these discrete peaks by DWBA, spectrum shapes described by the three models are similar to those shown in Fig. 16. For TTYs, the result obtained by the new method agrees well with the data. However, JQMD is not valid in this reaction system because of the absence of important nuclear reaction processes.

Fig. 22 shows angular dependence of TTYs in the deuteron-induced reaction on the ^{nat}C target for 40 MeV. Solid lines show results calculated by PHITS using INCL with DWBA, and closed circles represent experimental data [9]. Excellent agreement is observed between the calculated result and data, as in the reaction on the Li target, and the contribution to the spectra by DWBA is very effective in reproducing TTY data.

3.2.4. (d, xp) spectra on ^{nat}Li targets

DDXs at an emission angle of 0° in the inclusive (d, xp) reaction on the ^{nat}Li target for an incident energy of 40 MeV are shown in Fig. 23. The PHITS calculation was performed using targets of 0.86 mm thickness as in those shown in Section 3.2.1. INCL can describe the broad peak around the emitted proton of 20 MeV, by considering the neutron-stripping process. On the other hand, the spectrum obtained by JQMD does not have the peak. The difference between the results by INCL and JQMD is similar to that
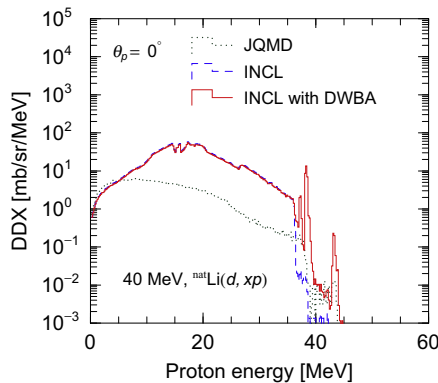
Fig. 23. DDXs in the $^{nat}Li(d, xp)$ reaction for 40 MeV at the 0° proton emission angle. Results calculated by PHITS with JQMD, INCL, and INCL with DWBA are denoted by dotted, dashed, and solid lines, respectively.

shown in the left panel of Fig. 16. The result calculated by the new method exhibits three discrete peaks at proton energies of 37, 38, and 43 MeV. The peaks at 37 and 38 MeV correspond to the DWBA results for the transitions to the first excited and ground states of ^8Li in the $^7Li(d,p)^8Li$ reaction, respectively. The peak at 43 MeV consists of discrete spectra of transitions to the ^7Li ground and first excited states in the $^6Li(d,p)^7Li$ reaction. Discrete spectra of the transitions to the other excited states in $^6Li(d,p)^7Li$ are not found in the spectrum, because of the small isotopic abundance of ^6Li to ^7Li in the ^{nat}Li target. Although no data of the proton spectrum for the 40-MeV incident energy are available, the new method is useful for reproducing the spectrum shape suggested by the data of Ref. [37].

3.2.5. (d, xp) spectra on ^9Be targets

Fig. 24 shows DDXs at the 3.5° proton emission angle in the $^9Be(d, xp)$ reaction for 18 MeV. The thickness of the target in the calculation is set to 0.015 mm. Spectrum shapes described by JQMD and INCL are similar to those shown in Fig. 19. Therefore, it is expected that INCL is more effective in estimating cross sections in the proton energy region below 15 MeV than JQMD. Discrete peaks in the spectrum calculated by the new method are observed at the energies of 16, 19, and 22.5 MeV. The right and middle peaks correspond to the transitions to the ground and first excited states of ^{10}Be in $^9Be(d,p)^{10}Be$, respectively. The DWBA cross sections for the transitions to the other four excited states contribute to the peak at 16 MeV. Because the $^9Be(d,p)^{10}Be$ reaction produces the emitted proton with higher energy than the incident deuteron energy, it is important for describing the proton spectra to consider discrete peaks obtained by DWBA.

3.2.6. (d, xp) spectra on ^{nat}C targets

DDXs at 0° in the $^{nat}C(d, xp)$ reaction for 40 MeV are shown in Fig. 25. In the PHITS calculation, we set the same thickness of the ^{nat}C target as that used in the calculation for the $^{nat}C(d, xn)$ reaction. Including the neutron-stripping process, INCL describes the broad peak at the 20-MeV proton energy, which cannot be obtained by JQMD. Four discrete peaks are found in the result calculated by the new method. Using DWBA, we considered the four and seven transitions for the ^{12}C and ^{13}C targets, respectively. The
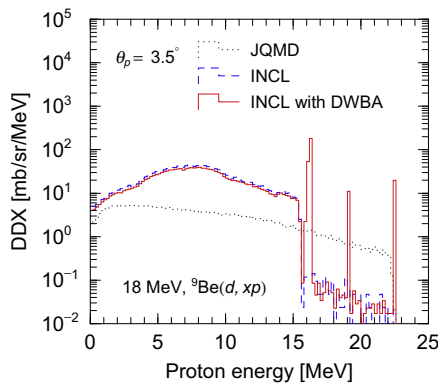
Fig. 24. DDXs at $\theta_p = 3.5°$ in ^{9}Be(d, xp) for 18 MeV. Dotted, dashed, and solid lines represent calculated results of PHITS with JQMD, only INCL, and INCL with DWBA, respectively.
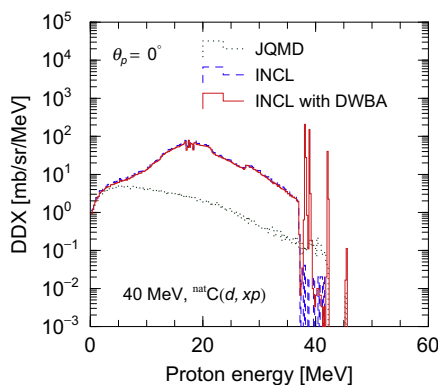
Fig. 25. DDXs at $\theta_p = 0°$ in the ^{nat}C(d, xp) reaction for the 40-MeV incident energy. Calculated results of PHITS with JQMD, only INCL, and INCL with DWBA, are represented by dotted, dashed, and solid lines, respectively.

peak at 38 MeV consists of discrete spectra of the two transitions to the ^{13}C second and third excited states in the ^{12}C$(d, p)^{13}$C reaction. The transitions to the ground and first excited states of ^{13}C correspond to the peaks at 39 and 42 MeV, respectively. In the ^{13}C$(d, p)^{14}$C reactions, only the discrete spectrum of the transition to the ^{14}C ground state is observed at 45 MeV, because the transition has higher Q-value than those on the ^{12}C target. The other discrete spectra of the transitions to the ^{14}C excited states have small contributions to the spectrum because of the isotopic abundance of ^{13}C to ^{12}C in ^{nat}C. As in the case of the ^{nat}C(d, xn) spectrum, PHITS with the new method can also describe the inclusive (d, xp) spectrum on the ^{nat}C target, which consists of the broad peak at half the incident energy and discrete peaks around the same proton energy as the incident deuteron.

4. Summary

We have proposed a new method that combines INCL and DWBA for describing the neutron and proton spectra of the deuteron-induced reaction in the Monte Carlo simulation for particle transport. The proposed method was incorporated into PHITS and applied to estimate the spectra for incident energy below 50 MeV on Li, Be, and C targets. Version 4.5 of INCL was used to describe most of the reaction process. Using the TWO-FNR code, the DWBA calculation was performed to obtain the (d, n) and (d, p) cross sections, resulting in discrete peaks in neutron and proton spectra, respectively. Both DDXs and TTYs in the (d, xn) reaction, calculated

by combining INCL and DWBA, successfully agree with experimental data, which cannot be reproduced by JQMD. The contribution of the discrete peaks to spectra is found at all emission angles. We also estimate DDXs in the (d, xp) reaction using the method. The spectra have similar features to the (d, xn) spectra, which exhibit broad peaks and some discrete peaks. In conclusion, the combined method is very useful to reproduce inclusive (d, xn) spectra, and the use of this method with PHITS will provide reliable results for estimating particle fluxes or dose distributions.

In the future, we plan to extend the applicable incident energy range and target nucleus. If the method can be used in the reaction for the energy up to 100 MeV, the research on the target design of neutron sources can be carried out in wider energy region. The information on neutron yields in collisions between scattered deuteron and materials in accelerators, is also important for accurately estimating particle fluxes in radiation fields. It should be noted that the validity of the method should be confirmed in these reactions. Improvements in the TWO-FNR code are necessary to consider residues in continuum states. Furthermore, the application of this framework to alpha spectra in deuteron-induced reactions or neutron spectra in proton-induced ones is an interesting prospect.

References

[1] A. Moeslang, V. Heinzel, H. Matsui, M. Sugimoto, The IFMIF test facilities design, Fusion Eng. Des. 81 (2006) 863.
[2] T. Sato, K. Niita, N. Matsuda, S. Hashimoto, Y. Iwamoto, S. Noda, T. Ogawa, H. Iwase, H. Nakashima, T. Fukahori, K. Okumura, T. Kai, S. Chiba, T. Furuta, L. Sihver, Particle and Heavy Ion Transport Code System PHITS, version 2.52, J. Nucl. Sci. Technol. 50 (2013) 913–923.
[3] M. Harada, N. Watanabe, C. Konno, S. Meigo, Y. Ikeda, K. Niita, DPA calculation for Japanese spallation neutron source, J. Nucl. Mater. 343 (2005) 197.
[4] H. Kumada, K. Yamamoto, A. Matsumura, T. Yamamoto, Y. Nakagawa, Development of JCDS, a computational dosimetry system at JAEA for boron neutron capture therapy, J. Phys. Conf. Ser. 74 (2007) 021010.
[5] T. Sato, K. Niita, Analytical Functions to Predict Cosmic-Ray Neutron Spectra in the Atmosphere, Radiat. Res. 166 (2006) 544.
[6] T. Sato, H. Yasuda, K. Niita, A. Endo, L. Sihver, Development of PARMA: PHITS-based Analytical Radiation Model in the Atmosphere, Radiat. Res. 170 (2008) 244.
[7] Y. Nara, N. Otuka, A. Ohnishi, K. Niita, S. Chiba, Relativistic nuclear collisions at 10A GeV energies from p+Be to Au+Au with the hadronic cascade model, Phys. Rev. C61 (1999) 024901.
[8] K. Niita, S. Chiba, T. Maruyama, H. Takada, T. Fukahori, Y. Nakahara, A. Iwamoto, Analysis of the (N, xN') reactions by quantum molecular dynamics plus statistical decay model, Phys. Rev. C 52 (1995) 2620.
[9] M. Hagiwara, T. Itoga, M. Baba, M.S. Uddin, N. Hirabayashi, T. Oishi, T. Yamauchi, Experimental studies on the neutron emission spectrum and activation cross-section for 40 MeV deuterons in IFMIF accelerator structural elements, J. Nucl. Mater. 329 (2004) 218.
[10] A. Boudard, J. Cugnon, S. Leray, C. Volant, Intranuclear cascade model for a comprehensive description of spallation reaction data, Phys. Rev. C66 (2002) 044615.
[11] J. Cugnon, D. Mancusi, A. Boudard, S. Leray, New features of the INCL4 model for spallation reactions, J. Korean Phys. Soc. 59 (2011) 955. and references therein.
[12] A. Boudard, J. Cugnon, J.-C. David, S. Leray, D. Mancusi, New potentialities of the Liège intranuclear cascade model for reactions induced by nucleons and light charged particles, Phys. Rev. C87 (2013) 014606.
[13] T. Ye, Y. Watanabe, K. Ogata, Analysis of deuteron breakup reactions on ^{7}Li for energies up to 100 MeV, Phys. Rev. C80 (2009) 014604.
[14] S. Hashimoto, Y. Iwamoto, T. Sato, K. Niita, A. Boudard, J. Cugnon, J.-C. David, S. Leray, and D. Mancusi, New approach for describing nuclear reactions based on intra-nuclear cascade coupled with DWBA, Prog. Nucl. Sci. Technol. (in press).
[15] T. Ye, S. Hashimoto, Y. Watanabe, K. Ogata, M. Yahiro, Analysis of inclusive (d, xp) reactions on nuclei from ^{9}Be to ^{238}U at 100 MeV, Phys. Rev. C84 (2011) 054606.
[16] M. Lacombe, B. Loiseau, J.-M. Richard, R. Vinh Mau, J. Côté, P. Pirès, R. de Tourreil, Parametrization of the Paris N–N potential, Phys. Rev. C21 (1980) 861.

[17] M. Kamimura, M. Yahiro, Y. Iseri, Y. Sakuragi, H. Kameyama, M. Kawai, Chapter I. Projectile breakup processes in nuclear reactions, Prog. Theor. Phys. Suppl. 89 (1986) 1.

[18] N. Austern, Y. Iseri, M. Kamimura, M. Kawai, G. Rawitscher, M. Yahiro, Continuum-discretized coupled-channels calculations for three-body models of deuteron-nucleus reactions, Phys. Rep. 154 (1987) 125.

[19] M. Igarashi, two-step finite-range DWBA code, TWOFNR, http://www.nscl.msu.edu/brown/reaction-codes/twofnr/twofnr.pdf (accessed July 4, 2013).

[20] H. Ohnuma, T. Kubo, N. Kishida, T. Hasegawa, N. Ueda, T. Fujisawa, T. Wada, K. Iwatani, T. Suehiro, Vector analyzing power and polarization measurements for the ^{116}Sn$(d, p)^{117}$Sn reaction and deuteron d-state effects, Phys. Lett. 97B (1980) 192.

[21] K. Hatanaka, N. Matsuoka, T. Saito, K. Hosono, M. Kondo, S. Kato, T. Higo, S. Matsuki, Y. Kadota, K. Ogino, Systematic study of the (d, p) reaction with 56 MeV polarized deuterons, Nucl. Phys. A419 (1984) 530.

[22] C.M. Bhat, Y. Tagishi, E.J. Ludwig, B.A. Brown, ^{36,38}Ar$(\vec{d}, \alpha)^{34,36}$Cl reactions induced by tensor polarized deuterons, Phys. Rev. C34 (1986) 736.

[23] X.D. Liu, M.A. Famiano, W.G. Lynch, M.B. Tsang, J.A. Tostevin, Systematic extraction of spectroscopic factors from ^{12}C$(d, p)^{13}$C and ^{13}C$(p, d)^{12}$C reactions, Phys. Rev. C69 (2004) 064313.

[24] S. Gangadharan, R.L. Wolke, Recoil Angular Distributions of the ^{6}Li$(d, n)^7$Be and ^{12}C$(d, n)^{13}$N Reactions, Phys. Rev. C1 (1970) 1333.

[25] J.P. Schiffer, G.C. Morrison, R.H. Siemssen, B. Zeidman, Study of the (d, p) Reaction in the 1p Shell, Phys. Rev. 164 (1967) 1274.

[26] S.E. Darden, G. Murillo, S. Sen, The ^{9}Be$(\vec{d}, d)^9$Be, ^{9}Be$(\vec{d}, p)^{10}$Be, ^{9}Be$(\vec{d}, t)^8$Be, AND ^{9}Be$(\vec{p}, d)^8$Be, REACTIONS AT 15 MeV, Nucl. Phys. A266 (1976) 29.

[27] Y. Han, Y. Shi, Q. Shen, Deuteron global optical model potential for energies up to 200 MeV, Phys. Rev. C74 (2006) 044615.

[28] B.A. Watson, P.P. Singh, R.E. Segel, optical-model analysis of nucleon scattering from 1p-shell nuclei between 10 and 50 MeV, Phys. Rev. 182 (1969) 977.

[29] S. Cohen, D. kurath, Spectroscopic factors for the lp shell, Nucl. Phys. A101 (1967) 1.

[30] S.G. Buccino, A.B. Smith, Levels in ^{10}B excited by the ^{9}Be(d, n) reaction, Phys. Lett. 19 (1965) 234.

[31] Y.S. Park, A. Niiler, R.A. Lindgren, Spectroscopy of ^{10}B Levels from the ^{9}Be$(d, n)^{10}$B Reaction, Phys. Rev. C8 (1973) 1557.

[32] G.S. Mutchler, D. Rendic, D.E. Velkey, W.E. Sweeney Jr., G.C. Phyllips, The (d, n) reaction on lp shell nuclei at E_d = 11.8 MeV, Nucl. Phys. A172 (1971) 469.

[33] H.R. Schelin, E. Farrelly Pessoa, W.R. Wylie, E.W. Cybulska, K. Nakayama, L.M. Facundes, R.A. Douglas, The ^{12}C$(d, n)^{13}$N reaction between E_d = 7.0 and 13.0 MeV, J. Nucl. Phys. A414 (1984) 67.

[34] E.W. Hamburger, J.R. Cameron, Study of some reactions of 14.8-MeV deuterons with the lithium isotopes, Phys. Rev. 117 (1960) 781.

[35] H. Ohnuma, N. Hoshino, O. Mikoshiba, K. Raywood, A. Sakaguchi, G.G. Shute, B.M. Spicer, M.H. Tanaka, M. Tanifuji, T. Terasawa, M. Yasue, The ^{12}C$(d, p)^{13}$N reaction at E_d = 30 MeV and positive-parity states in ^{13}C, Nucl. Phys. A448 (1985) 205.

[36] R.J. Peterson, H.C. Bhang, J.J. Hamill, T.G. Masterson, The ^{14}C$(\alpha, \alpha')^{14}$C AND ^{13}C$(d, p)^{14}$C reactions, Nucl. Phys. A425 (1984) 469.

[37] D. Ridikas, W. Mittig, H. Savajols, P. Roussel-Chomaz, S.V. Förtsch, J.J. Lawrie, G.F. Steyn, Inclusive proton production cross sections in (d, xp) reactions induced by 100 MeV deuterons, Phys. Rev. C63 (2000) 014610.

[38] M. Hagiwara, T. Itoga, N. Kawata, N. Hirabayashi, T. Oishi, T. Yamauchi, M. Baba, M. Sugimoto, T. Muroga, measurement of neutron emission spectra in Li(d, xn) reaction with thick and thin targets for 40-MeV deuterons, Fusion Sci. Technol. 48 (2005) 1320.

[39] A.K. Weaver, J.D. Anderson, H.H. Barschall, J.C. Davis, Neutrons from the bombardment of beryllium by deuterons, Phys. Med. Biol. 18 (1973) 64.

[40] Y. Iwamoto, Y. Sakamoto, N. Matsuda, Y. Nakane, K. Ochiai, H. Kaneko, K. Niita, T. Shibata, H. Nakashima, Measurements of double-differential neutron-production cross-sections for the ^{9}Be(p, xn) and ^{9}Be(d, xn) reactions at 10 MeV, Nucl. Instr. Meth. A 598 (2009) 687.